Influence of preoxidation on high temperature corrosion of a Ni-based alloy under conditions relevant to biomass firing

Okoro, Sunday Chukwudi; Montgomery, Melanie; Jappe Frandsen, Flemming; Pantleon, Karen

Published in:
Surface and Coatings Technology

Link to article, DOI:
10.1016/j.surfcoat.2017.03.068

Publication date:
2017

Document Version
Peer reviewed version

Influence of preoxidation on high temperature corrosion of a Ni-based alloy under conditions relevant to biomass firing

Sunday Chukwudi Okoro[1, 2*], Melanie Montgomery[1], Flemming Jappe Frandsen[2], Karen Pantleon[1]

[1] Technical University of Denmark (DTU), Department of Mechanical Engineering, 2800 Kongens Lyngby, Denmark.

[2] Technical University of Denmark (DTU), CHEC Research Centre, Department of Chemical and Biochemical Engineering, 2800 Kongens Lyngby, Denmark.

*Corresponding author. Phone: +45 50185680, Email: sunoko@kt.dtu.dk, okorochukwudi@ymail.com.

Abstract

Development of corrosion resistant materials in biomass fired power plants demands specific attention since the condensation of deposits rich in KCl on heat exchanger surfaces induces severe corrosion attack, which is different from corrosion in traditional coal fired plants. Therefore, the ability of preoxidized layers formed on a commercial Cr-Ti-Al-containing Ni-based alloy (Nimonic 80A) to withstand biomass-induced corrosion was investigated. Preoxidation treatments at 900 °C in O_2 and O_2 + 10 vol % H_2O, respectively, were conducted before samples were exposed to conditions that mimicked biomass firing. Complementary characterization methods were employed to study samples after preoxidation as well as after corrosion exposure. The oxides obtained by the preoxidation treatments protected the alloy during corrosion exposure at 560 °C for a period of 168 h. In contrast, non-preoxidized samples suffered corrosion attack and formed porous non-protective oxides containing the alloying elements, Ni, Cr, Ti and Al. The influence of the preoxidation layers on the corrosion mechanism is discussed.

Keywords: High temperature corrosion, Biomass firing, Preoxidation, KCl, Chlorination, TiO_2.

1. Introduction

High temperature corrosion is a serious problem for biomass fired power plants due to the condensation of corrosive KCl rich deposits on the heat exchanger surfaces (such as superheaters) [1–3]. This arises mainly from the high content of organically bound K and Cl in biomass, which during combustion, become devolatilized and condense as deposits rich in K and Cl [4,5]. To handle the corrosion problem in biomass fired plants, the maximum operation steam temperature is limited to low values (usually below 540 ^{o}C), thereby limiting the electrical efficiency of biomass fired power plants. Identification of materials with improved corrosion resistance for use as superheaters in biomass fired power plants is therefore of utmost importance [6].

Recent investigations have shown that without any dedicated surface modification, chromia and alumina forming alloys do not give adequate protection in the presence of alkali chlorides (see for example [6–12]). One of the principal factors responsible for this is the thermodynamic favourability of the reaction between alloying elements and chlorine, leading to formation of volatile metal chlorides which are then oxidized to form non-protective oxides [13]. Consequently, the protective ability of coatings containing possible protective elements have been investigated under conditions related to biomass firing [14–19]. However, the inter-diffusion of alloying elements as well as the possibility of corrosive species to diffuse through the coating splat boundaries [18] are vital factors to be considered if coatings are to be applied for protection of superheaters against alkali chloride induced corrosion.

Surface modification employing the materials own alloying elements for the formation of protective oxides at the surface prior to corrosion exposure (i.e. preoxidation) provides an avenue for rendering protection to materials under aggressive conditions. This approach has been widely investigated under sulphidation conditions [20–24], and in a few cases, under conditions related to biomass firing [25–29]. With respect to investigations related to biomass firing, the effect of preoxidation for protection against corrosion depends on the composition and crystallography of the preoxidized layer, preoxidation conditions, as well as the corrosive environment [29]. In particular, a positive effect of preoxidation of pure Cr and Ni against HCl has been reported while pure Fe preoxidized under similar conditions suffered corrosion [29]. Similarly, the resulting Al_2O_3 from preoxidation of a commercial FeCrAl alloy has been reported to give some degree of protection against KCl induced corrosion attack [26]. Furthermore, an investigation with chromia forming alloys (EN 1.4982, EN 1.4301 and EN 1.4845) revealed a positive effect of preoxidation against attack by HCl at low temperatures (400 ^{o}C) [28]. On the other hand, no positive effect was reported for preoxidation of Fe-30Cr alloys in oxygen, when they were subsequently exposed to a gaseous KCl environment [27]. This implies that although Cr-oxide rich preoxidation layers may be resistant to attack by HCl [28,29], they can exhibit poor resistance to KCl-induced attack [27], possibly due to the reaction between KCl and Cr_2O_3 [30].

Investigations of the reactivity of a number of oxides and KCl under oxidizing conditions have indicated that KCl does not react with TiO_2, ZrO_2, Y_2O_3, Ta_2O_5, HfO_2, Al_2O_3, NiO, Fe_2O_3, CeO_2 and Co_3O_4 [31]. These results suggest that alloys with the capability of forming such oxides may

experience limited corrosion attack under biomass-firing conditions. Based on this and with the need for further exploration of preoxidation as an avenue for corrosion protection under biomass firing conditions, the present work reports on the influence of preoxidation on the corrosion resistance of a Cr-Al-Ti-containing Ni-based alloy (Nimonic 80A) under laboratory conditions mimicking biomass firing.

2. Experimental procedures

2.1 Sample preparation, preoxidation and high temperature corrosion exposures

The investigated material was a Ni-based alloy (Nimonic 80A). Its chemical composition as determined by Energy Dispersive X-ray Spectroscopy (EDS), is as follows (in wt%): Al-1.3, Ti-2.2, Cr-20.6, with Ni as balance. Using fusion thermal conductivity detection units, LECO CS230 and LECO TN500, the carbon and nitrogen contents of the alloy amounts to 0.070 wt% C and 0.014 wt% N [7]. Arc shaped samples having an external arc length of 23.6 mm were obtained from the tube material with a precision cut-off machine (Struers, Accutom-50). The samples were ultrasonically cleaned and dried in acetone and ethanol, before they were subjected to the various heat treatments, which are summarized in Table 1.

Table 1. Summary of the different heat treatment conditions in the present study

Experiments	Temperature (°C)	Time (h)	Atmosphere
Preoxidation I	900	168	O_2
Preoxidation II	900	168	O_2 + 10 vol% H_2O
Annealing	900	96	Ar
Corrosion exposures[(a)]	560	168	KCl deposit + 400 ppmv HCl, 60 ppmv SO_2, 12 vol% CO_2, 6 vol% O_2, 3 vol % H_2O, N_2-balance

[(a)] with the exception of H_2O, gas compositions are given on a dry basis.

The various heat treatments consist of preoxidation or annealing in inert gas atmosphere and subsequent corrosion exposure. Preoxidation in oxidizing atmospheres was carried out in either O_2 (preoxidation-I) or O_2 with the addition of 10% water vapour (preoxidation-II) to form surface oxides. Annealing in inert atmospheres aimed to investigate possible temperature induced changes of the bulk microstructure. Finally, corrosion exposure of the different samples was carried out under conditions that mimic the environment experienced by superheaters in biomass fired power plants. To this end, a slurry of KCl in isopropanol was used to obtain an about 1mm thick KCl deposit on each sample before its exposure to the corrosive gases in a dedicated corrosion test rig (for details about the test rig, see [32]). The KCl deposit together with the applied gas mixture containing HCl, SO_2, CO_2, O_2, H_2O and N_2 according to Table 1 mimics biomass firing. All experiments were conducted isothermally and samples were subsequently allowed to cool under their respective gaseous

atmospheres applied for the treatment. At least three samples in either the as-received, preoxidized or annealed condition have been exposed to high temperature corrosion and investigated afterwards.

2.2 Characterization of samples

Light optical microscopy (LOM), scanning electron microscopy (SEM), energy dispersive X-ray spectroscopy (EDS) and X-ray diffraction (XRD) were employed for sample characterization.

Cross sections of the as-received, preoxidized and annealed samples were mounted in an epoxy resin and prepared by grinding and polishing down to 1 µm diamond suspension according to standard metallographic procedures. For characterization of the bulk microstructure of the as-received (non-preoxidized), preoxidized and annealed samples, prior to and after corrosion exposures, cross sections of these samples were etched with glyceregia before microstructure analysis using LOM (OLYMPUS GX 41). The cross sections of all samples exposed to the corrosive conditions were carefully prepared under water free conditions. Details of this procedure are described elsewhere [32]. These cross sections were analysed with SEM (Inspect S or Quanta ESEM FEG, FEI) and EDS (Oxford instruments) using an acceleration voltage of 15 keV. SEM investigations were conducted with both backscattered electron (BSE) and secondary electron (SE) detectors to obtain information on variations of both chemical composition and morphology. From the obtained SEM images, the thicknesses of the preoxidation layers and corrosion products were measured using the image analysis software ImageJ. Over 50 measurements were carried out for each set of samples to meet statistical requirements for the thickness distribution of the formed surface layers.

In addition to the conventional mapping of cross sections by EDS, an elemental re-quantification method (previously described in [33]) was employed to obtain an averaged one-dimensional representation of depth-profiles of relevant chemical elements. This involved subdivision of the mapped regions into strips of meshes in directions parallel to the sample surface, and subsequent re-quantification (from the acquired EDS map data) of the average composition of elements in these meshes using the INCA software (Oxford instruments). Generally, the length of these meshes (in the direction parallel to the surface of the sample) was over 100 µm, corresponding to the length of the micrograph. However, due to the difference in thickness of the oxides obtained from preoxidation, and the reaction products obtained after corrosion exposures, different widths of the meshes were employed. For the relatively thick oxides on the preoxidized samples, a mesh width of 1.5 µm was applied, while a 0.5 µm wide mesh was used to properly capture the chemical variations in corrosion products observed on non-preoxidized samples. The elemental profiles were then obtained by plotting the re-quantified averaged compositions from each strip of mesh, as a function of distance in the direction perpendicular to the interface between the oxide (or corrosion product) and the alloy.

Plan view investigations using SEM, EDS and XRD were also carried out to supplement the analysis of the cross sections. For corrosion exposed samples, plan view investigation involved careful successive removal of the corrosion products, starting from the deposit/gas interface, and characterization of the exposed interfaces (for details, see [34]). In all the plan view investigations, a diffractometer (Bruker AXS, D8 Discover) equipped with Cr-Kα radiation was applied for XRD measurements. To limit the X-ray penetration depth, measurements were carried out in grazing

incidence geometry (GI-XRD) using a fixed incidence angle ($\gamma = 2^o$ for analysis of preoxidation layers, and 5^o for corrosion product analysis). A counting time of 10 sec per detector step of 0.03 $^o2\theta$ was employed for all XRD measurements.

3 Results

3.1 Morphology and composition of preoxidation layers

Results of microscopy and chemical analysis of the oxide surfaces after preoxidation of Nimonic 80A at 900 ^{o}C in O_2 (preoxidation I), and in O_2 + 10 vol% H_2O (preoxidation II), are shown in Figures 1 and 2, respectively. After preoxidation in either atmosphere (H_2O or H_2O+O_2), both preoxidation layers were similarly enriched in Cr and Ti, with local Ti rich agglomerates (Figures 1a and 2a). The preformed oxide in both atmospheres consisted of: i) an outer layer, containing some voids as well as discrete features with a lower atomic weight, and, ii) an internal oxidation zone, which contained features with an acicular microstructure (Figures 1b and 2b). Oxidation along alloy grain boundaries was commonly observed within the internal oxidation zone. Figures 1b and 2b also show that the alloy contains Ti-N rich and Cr-rich precipitates. While the Ti-N precipitates were present in the as-received alloy, the Cr-rich precipitates only became apparent after the preoxidation treatment (see section 3.2.3). Within the internal oxidation zone, both types of precipitates were absent.

The EDS maps in Figures 1c and 2c clearly reveal a similar composition for the layers resulting from preoxidation I and II, suggesting that the result of preoxidation does not depend on the applied atmosphere. The outer layer comprises of Ti and Cr rich oxide, with Ti being enriched in the outermost regions of the oxide and also as discrete precipitates in the outer layer. The acicular features in the internal oxidation zone are identified as Ti and Al-rich oxides. Oxides along alloy grain boundaries are enriched in Ti, Al and, in some regions, in Cr. For a sample from preoxidation I, the elemental profiles in Figure 3 reveal quantitatively that Ti and Cr are enriched in the outer layer while Cr is depleted in the internal oxidation zone within which enrichment of Al and Ti is evident.

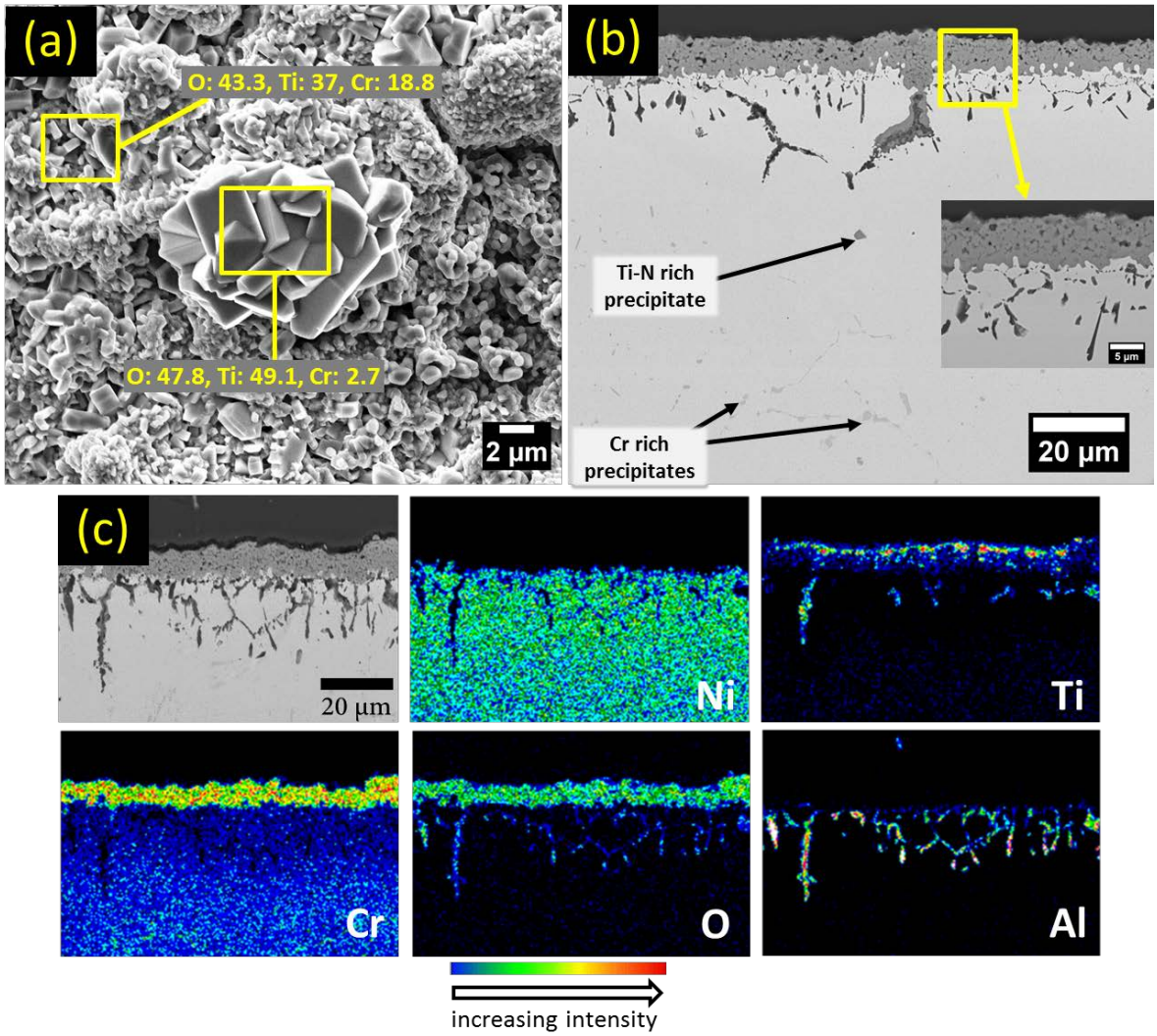

Figure 1. Microstructure of the oxide resulting from preoxidation in O_2. (a) SE micrograph showing the plan view morphology of the oxide. (b) BSE micrographs showing the cross section of the sample after preoxidation. (c) EDS maps showing the elemental distribution within the oxide. The inserted EDS results in (a) are given in wt%.

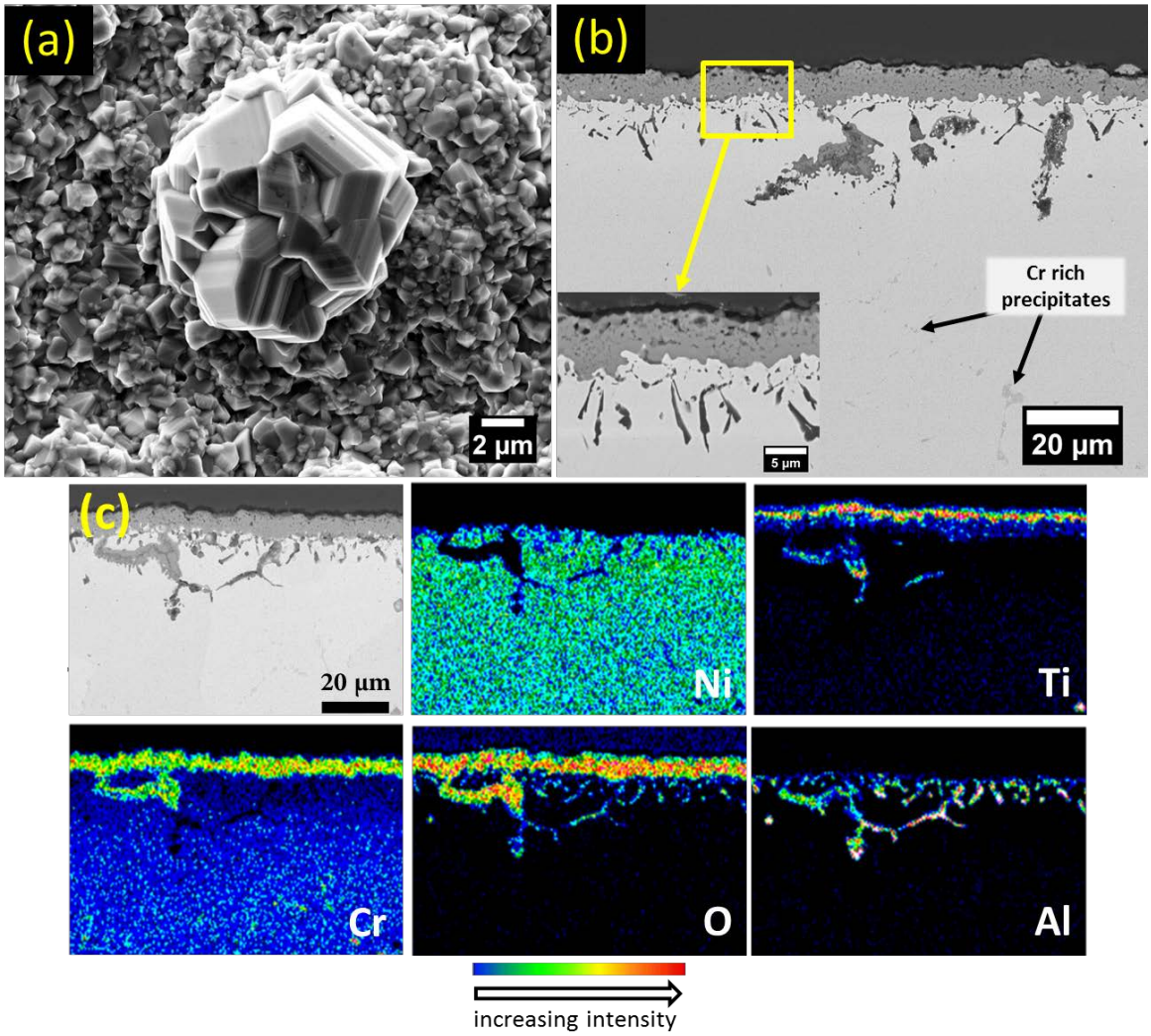

Figure 2. Microstructure of the oxide resulting from preoxidation in O_2 + 10 vol% H_2O. (a) SE micrographs showing the plan view morphology of the oxide. (b) BSE micrographs showing the cross section of the sample after preoxidation. (c) EDS maps revealing the elemental composition of the oxide.

In line with EDS results (Figures 1c, 2c and 3), phase analysis by means of XRD (Figure 4) revealed that the oxides formed after preoxidation I and II have similar phase composition. The presence of TiO_2 (Rutile, according to Joint Committee on Powder Diffraction Standards, JCPDS card: 21-1276) is clearly detected, with an additional oxide either consisting of Cr_2O_3 (JCPDS card: 38-1479) and/or a solid solution of Ti in Cr-oxide $(Cr_{0.88}Ti_{0.12})_2O_3$ (JCPDS card: 82-0211).

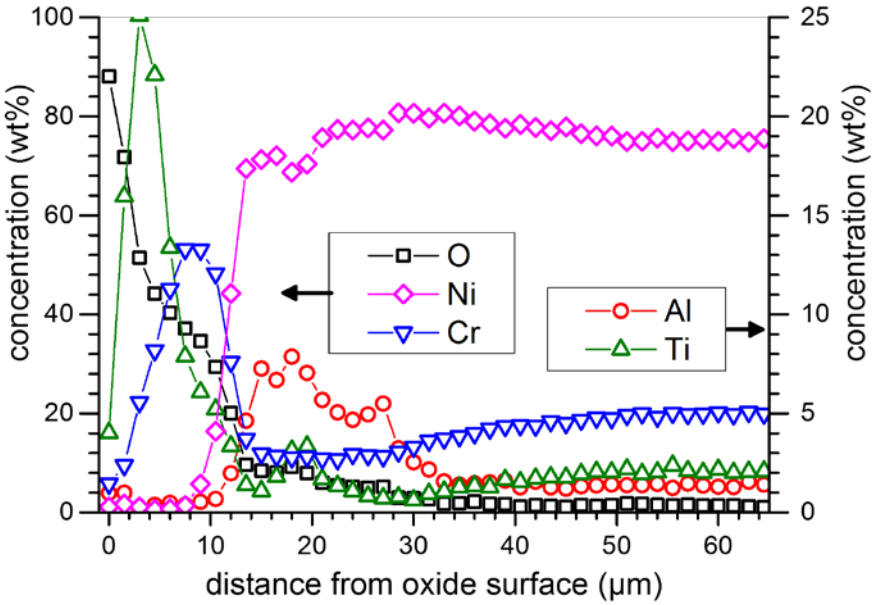

Figure 3. Elemental profiles showing variation in the average elemental composition obtained from re-quantification of EDS maps covering the preoxidation layer and the bulk alloy on samples preoxidized in O_2 (preoxidation I). Note the difference in the horizontal scales.

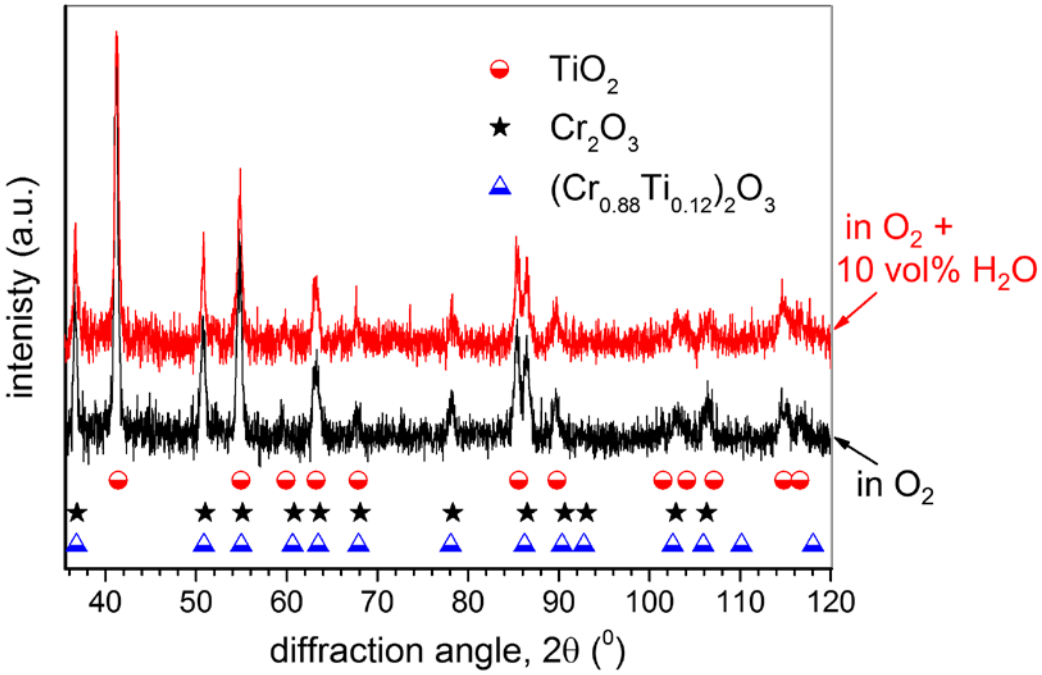

Figure 4. XRD patterns showing the crystalline phases present in the oxidized layers under different conditions of preoxidation.

Table 2. Average thickness of the outer layer (OL) and inner oxidation zone (IOZ) resulting from the different preoxidation treatments.

Preoxidation treatment	Average thickness (μm)	
	OL	IOZ
Preoxidation I	9 ± 2	14 ± 8
Preoxidation II	7 ± 1	11 ± 6

With over 50 measurements on the sample cross section, the statistical distribution of the thickness of the outer layer and internal oxidation zone, as summarized in Table 2, indicate similar thicknesses for the respective layers after sample treatment under the different preoxidation conditions.

3.2 Results from corrosion exposures

3.2.1 Corrosion attack on non-preoxidized samples

Figure 5 presents the microstructure and elemental composition of the corrosion products observed after exposure of non-preoxidized samples to the simulated biomass firing conditions. The micrograph in Figure 5a reveals that the corrosion product consisted of a highly porous oxide located above the bulk alloy. In addition, localized pores/voids are observed at the corrosion front. It is observed that Cr-rich precipitates are detected in the bulk of the non-preoxidized sample after the corrosion exposure (Figure 5a). The elemental maps in Figure 5b show that the upper layer of the corrosion product above the porous oxide consists mainly of K, S and O. Its morphology suggests that this layer has been molten during exposure. Additionally, Cr and Ni rich precipitates are present in this layer. The porous oxide below this is revealed to consist of Ni, Cr, Ti, Al and O (Figure 5b). In particular, Ti and Al are enriched in the lower regions of the porous oxide, i.e. closer to the bulk alloy. The elemental profiles generated from the elemental re-quantification method (Figure 5c) started from the interface between the molten K,S,O rich layer and porous oxide and progressed into the bulk alloy, and reveal that Cr, Ti and Al are enriched in the innermost region of the porous oxide. In between the porous oxide region and the bulk alloy, these elements are depleted resulting in the observed enrichment of Ni.

Results from plan view investigations coupled with mechanical removal of the deposit layer, show that large K, S and O rich agglomerates formed on the original KCl deposit particles, both at the deposit/gas (Figure 6a) and deposit/corrosion product (Figure 6b) interfaces. The observation of such features at the latter interface is in agreement with the K, S and O rich layer above the porous oxide observed on the sample cross section (cf. Figure 5). In addition, minor amounts of Cr and Ni were identified together with the K, S and O rich features at the deposit/alloy interface (Figure 6b).

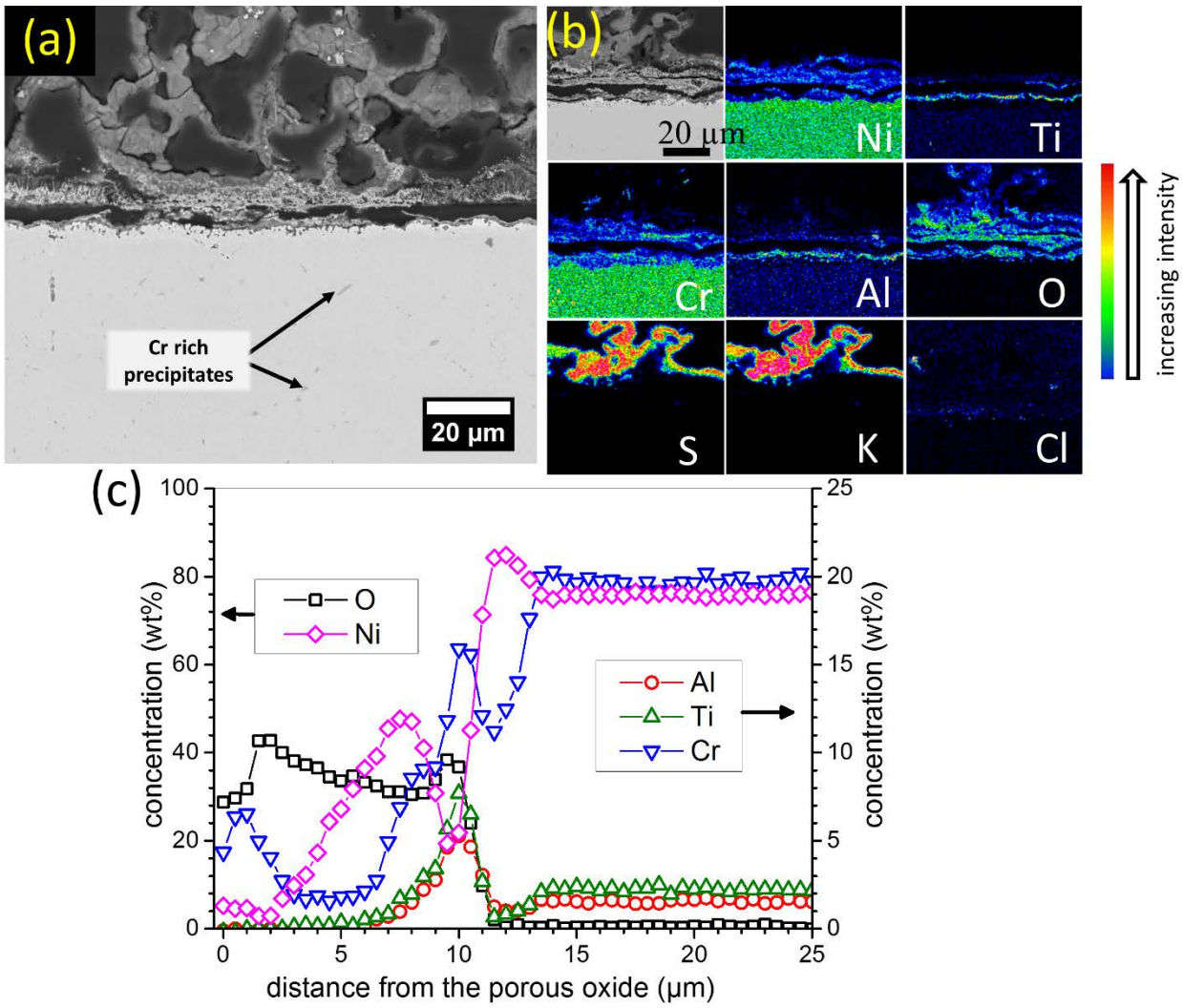

Figure 5. Microstructure of the corrosion product resulting from corrosion exposure of a non-preoxidized sample. (a) BSE micrographs showing the cross section of the corrosion product. (b) EDS maps revealing the elemental composition of the corrosion product. The re-quantified elemental profiles in (c) show the variation in average elemental composition starting from the interface between the molten K,S,O rich layer and porous oxide part of the corrosion product, towards the bulk alloy.

Phase analysis by XRD (not shown here) revealed that the crystalline phases at these interfaces include both the deposit, i.e. the original KCl (JCPDS card: 41-1476), and its transformation to K_2SO_4 (JCPDS card: 70-1488), thus accounting for the K, S and O rich layer. Compared to plan view investigations, KCl was not detected in prepared cross-sections and this could indicate that the compound was removed during preparation, even though absolute alcohol was used as lubricant instead of water during preparation. The plan view microstructure of the Ni, Cr, Ti, Al and O rich porous layer of the corrosion product located below the K_2SO_4-rich layer is shown in Figure 6c. The

very porous nature of this layer is also evident from the micrograph in Figure 6d which shows plan view microstructure of some needle-like porous Ni-rich regions of the corrosion product.

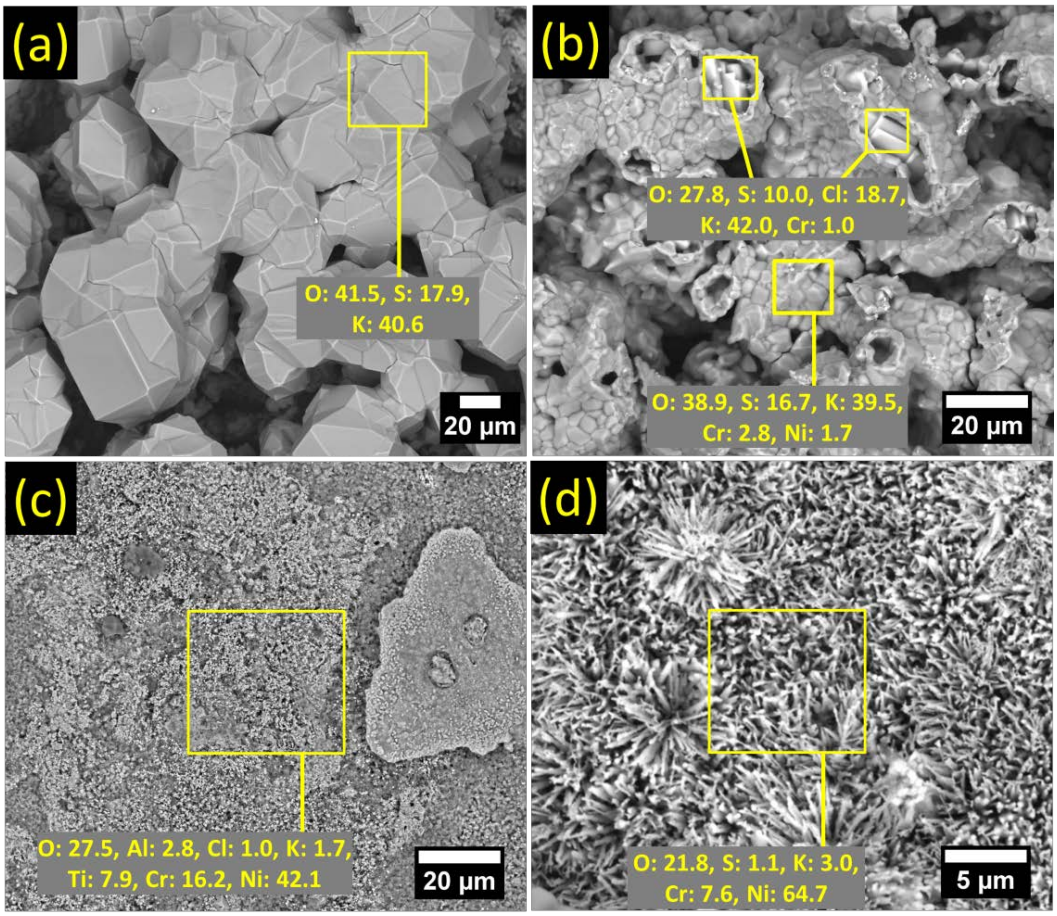

Figure 6. BSE micrographs showing the plan view microstructure of the corrosion product resulting from corrosion exposure of a non-preoxidized sample. (a) The deposit appearance from the gas/deposit and (b) deposit/oxide interfaces. (c and d) The plan view microstructure of the porous corrosion product layer observed after removal of the deposit and the K_2SO_4-rich layer. Elemental compositions are given in wt %.

3.2.2 Corrosion of preoxidized samples

No significant change in the morphology of the oxides obtained from the different preoxidation treatments (I and II) could be observed after their exposure to conditions simulating biomass firing. Figures 7 and 8 present the microstructure and elemental composition of preoxidized samples, illustrated with the example of a sample preoxidized in O_2 (preoxidation I).

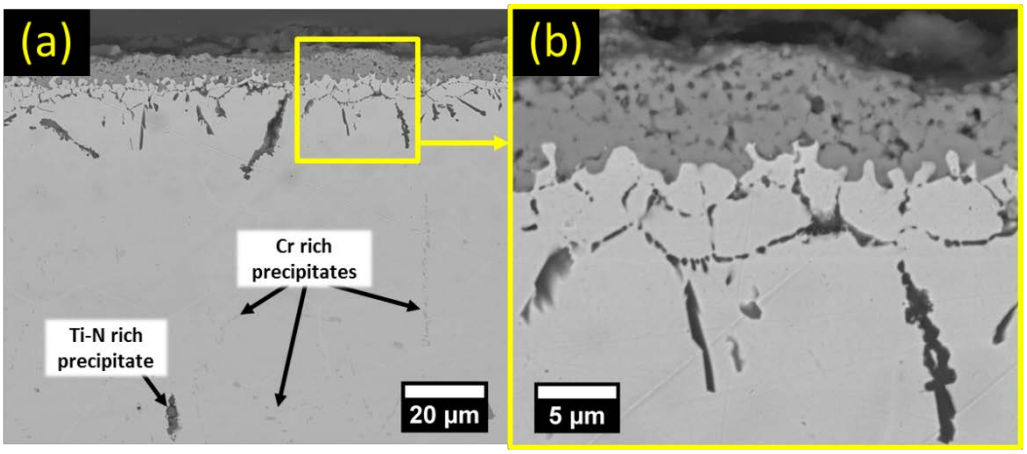

Figure 7. Microstructure of a sample preoxidized in O_2 after its exposure to corrosion conditions.

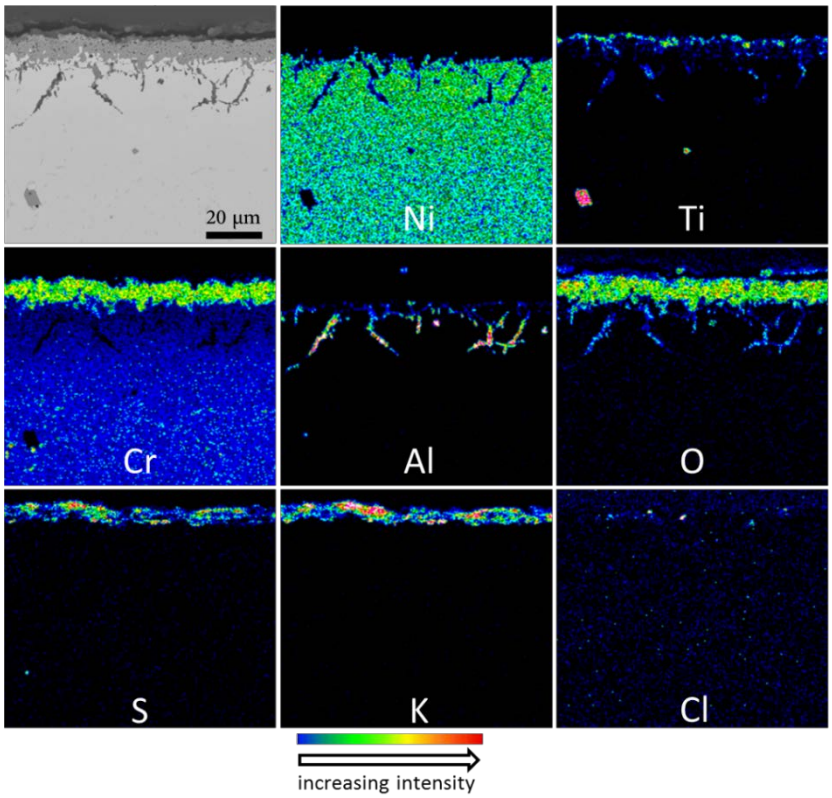

Figure 8. EDS maps showing elemental composition on the cross section of the sample preoxidized in O_2 after its exposure to corrosion conditions.

Apart from the presence of K and S on the surface (Figure 8), the elemental composition of the oxide remained unchanged after the corrosion exposure. The presence of the Ti and Cr rich outer layer as well as the Ti and Al rich oxide within an internal oxidation zone, was still evident after the corrosion exposure.

Furthermore, comparison of the element depth-profiles across the preoxidized samples before (cf. Figure 3) and after the corrosion exposure (Figure 9) reveals no qualitative difference in elemental

composition of the preoxidation layer. Based on the statistical representation of the thickness of the different oxide layers, as shown in Figure 10, it is also observed that both the average thickness of the outer oxide and the internal oxidation zone of the preoxidized samples were not affected by the corrosion exposure.

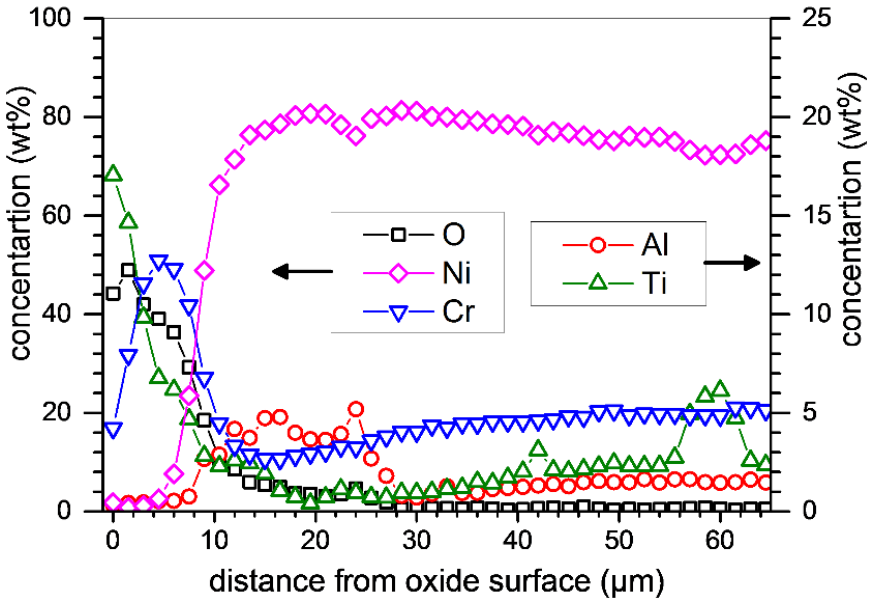

Figure 9. Elemental profiles showing variation in average elemental composition, starting from the outermost region of the preoxidation layer towards the bulk alloy, on a sample preoxidized in O_2 after their exposure to corrosion conditions mimicking biomass firing. The spikes in Ti concentration within the bulk alloy (at 42 µm and 60 µm) are due to the presence of Ti-rich precipitates. Note that K and S observed above the outermost region of the preoxidation layer are not shown in the plot.

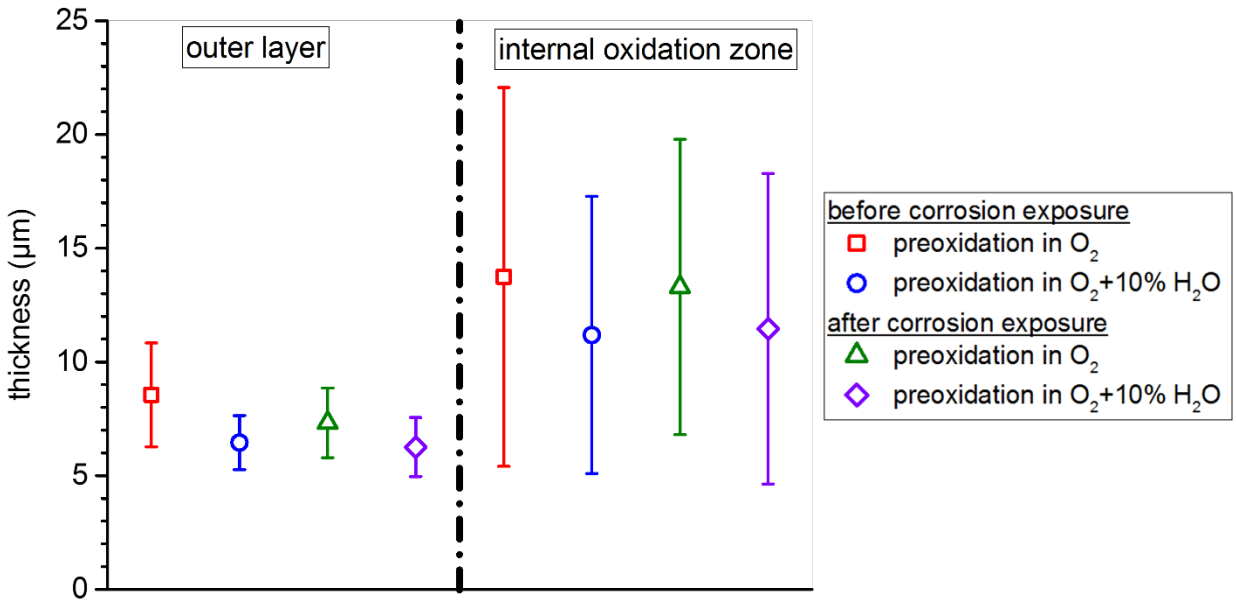

Figure 10. Oxide layer thicknesses after preoxidation in O_2 and in O_2 + 10% H_2O, and after corrosion exposure of the preoxidized samples.

To further understand the resistance of the preoxidized samples to corrosion attack observed on cross sections (Figure 7), plan view characterization including stepwise removal of the deposit, was additionally conducted. As shown in Figures 11a and b, K, S, O rich features accumulated around the KCl deposit particles, both at the deposit/gas (Figure 11a) and at the deposit/alloy interfaces (Figure 11b), similar to observations on non-preoxidized samples (cf. Figures 6a and b). However, the size and degree of coverage of the deposit particles by these K, S and O rich features is less, compared to the deposits on the non-preoxidized samples (cf. Figure 6a and b). As a result, substantial amounts of Cl (> 20 wt %) were detected by EDS analysis on these features. In line with EDS results in Figure 11a and b, both KCl (JCPDS card: 41-1476), and K_2SO_4 (JCPDS card: 70-1488) were identified by XRD at the gas/deposit and deposit/alloy interfaces (diffractograms not shown here). No porous oxide was observed after removal of the deposits on preoxidized samples. Instead, fragments of K and Cl rich features (possibly deposit particles) on a sulphate layer were present above the preoxidation layer (Figure 11c). Upon successive mechanical removal of the sulphate rich layer in Figure 11c, only the Cr and Ti rich outer layer of the initially formed oxide (Figure 11d) and Ti and Al enriched features in the internal oxidation zone (Figure 11e) were observed.

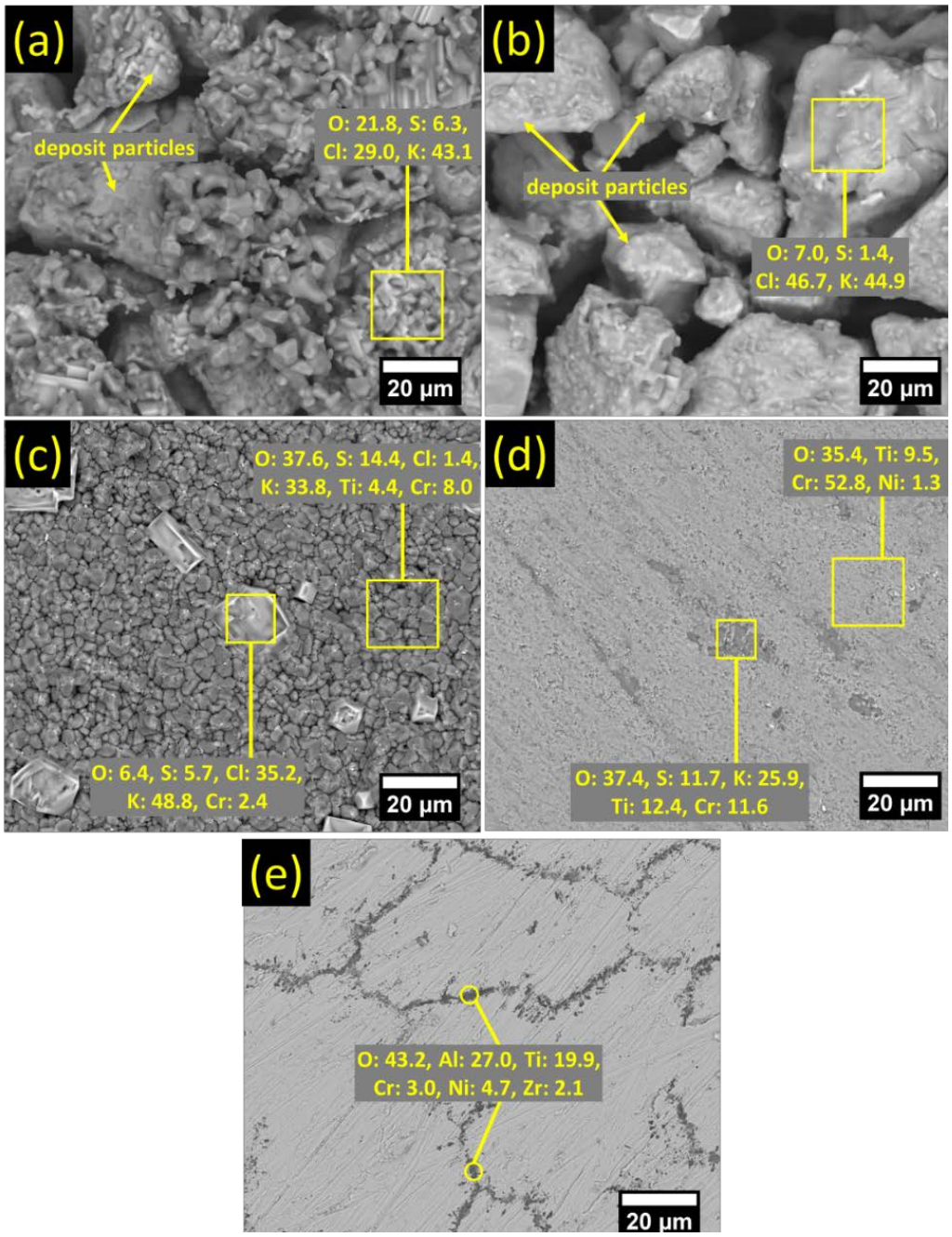

Figure 11. BSE micrographs showing the plan view microstructure of the corrosion product resulting from corrosion exposure of preoxidized samples. (a) The deposit appearance from the gas/deposit and (b) deposit/oxide interfaces. (c) Plan view microstructure of the corrosion product directly below the deposit. The micrographs in (d) and (e) show the microstructure of the Cr-Ti rich oxide and the internal oxidation zone respectively, following successive mechanical removal of the preceding layers. Elemental compositions are given in wt %.

3.2.3 Changes in bulk microstructure and corrosion of annealed samples

The bulk microstructure of the non-preoxidized and preoxidized samples was investigated with LOM following etching of cross sections with glyceregia. As shown in Figure 12a, only Ti-rich precipitates

are present in the as-received state of the alloy. Although SEM analysis revealed the presence of Cr-rich precipitates after corrosion exposure of non-preoxidized samples (Figure 5a), LOM investigations (Figure 12b) show that at 560 ^{o}C these precipitates are not so pronounced compared to their distribution after the preoxidation treatment at 900 ^{o}C (Figure 12c). Evidently, preoxidation at 900 ^{o}C promoted the formation of Cr-rich precipitates and, in addition, modified the bulk microstructure of the alloy with respect to its grain size. This may have consequences for the diffusion of alloying elements during the subsequent corrosion exposure, such that the observed resistance of the preoxidized samples to corrosion may be either due to the modified microstructure of the bulk alloy, or an effect of the preoxidation layer. To isolate these effects, prior annealing of non-preoxidized samples under inert atmospheres (argon, Ar), at 900 ^{o}C for 96 h was conducted to provoke a bulk microstructure (Figure 12d), similar to that after the preoxidation treatments. The annealed samples were finally subjected to corrosion exposure under conditions mimicking biomass firing.

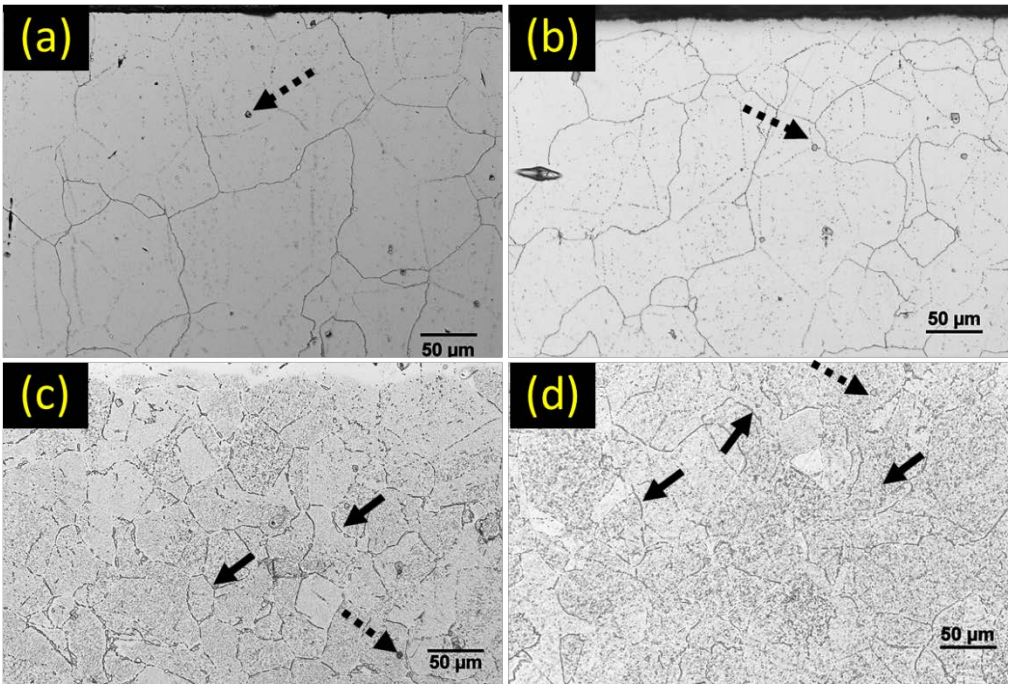

Figure 12. Optical micrographs showing the bulk microstructure of (a) the investigated alloy in the as-received condition, (b) a non-preoxidized sample after corrosion exposure (560 °C, 168 h), (c) a sample preoxidized in O_2 at 900 ^{o}C, 168 h and (d) a sample annealed in Ar at 900 ^{o}C, 96 h. Dotted arrows indicate the location of Ti-rich precipitates while solid arrows mark Cr-rich precipitates in the alloy.

Figure 13 show that the annealed samples suffered similar corrosion attack as the non-preoxidized samples (cf. Figure 5 and Figure 13). The outer part of the corrosion product on the annealed samples consisted of a K, S and O rich heterogeneous layer with Cr and Ni rich particles. Below this, there was a continuous, but porous layer in which Ni is essentially enriched in the outer regions (Figure 13b), while Cr, Ti and Al are enriched in the inner regions (closer to the bulk alloy). This observed

similarity between the corrosion attack on the annealed and non-preoxidized samples strongly indicates that the resistance of the preoxidized samples to corrosion attack is due to the presence of the preoxidation layer and not due to the change in bulk microstructure of the alloy induced by the heat treatments.

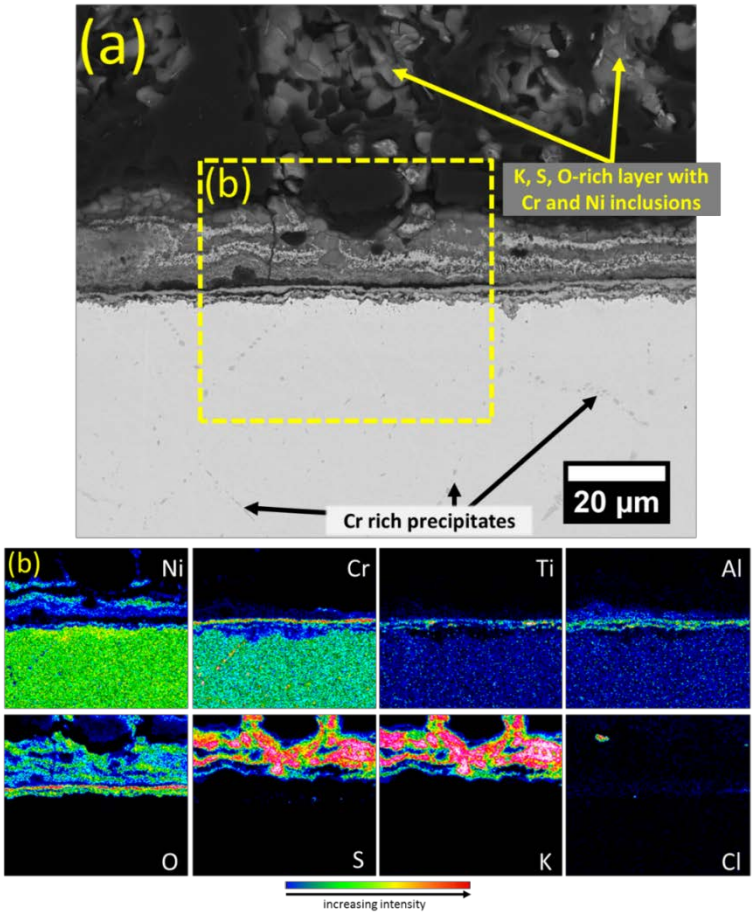

Figure 13. Microstructure of the corrosion product resulting from corrosion exposure of a sample initially annealed in Ar at 900 ºC. (a) BSE micrographs showing cross sections of the corrosion product. (b) EDS maps showing the elemental composition of the region highlighted in (a).

4 Discussion

The preoxidation treatment of Nimonic 80A resulted in an outer layer of oxide, identified by XRD (Figure 4) and SEM-EDS to contain both TiO_2 and Cr_2O_3. In addition, an internal oxidation zone, in which Al, Ti and Cr were oxidized (Figures 1c and 2c), developed above the bulk alloy. The observed microstructure and oxide composition after preoxidation are typical for Ni-Cr-Al alloys [35,36], because the high content of Cr in the alloy (20.6 wt %) can facilitate the growth of an external Cr_2O_3 layer after development of the transient Ni-Cr-Al-rich oxide [36]. Cr_2O_3 rich layers are prone to degradation in water vapour containing atmospheres due to evaporation of Cr from the oxide in the form of oxyhydroxides [37,38], but interestingly, such effect was not clearly observed in the present study due to the similar morphology and composition of the layers obtained after preoxidation in O_2 and in O_2 + 10 vol% H_2O (Figures 1 and 2). The low concentration of Al (1.3 wt %) in the alloy

cannot facilitate the formation of a continuous Al_2O_3 layer, hence, Al was internally oxidized, both as discrete particles (the acicular features in Figures 1b and 2b) and along the grain boundaries of the alloy. In addition, the low oxygen partial pressure (p_{O_2}) in equilibrium with Al_2O_3 will support internal oxidation of Al, and by a similar consideration, the internal oxidation of Ti, below the Cr_2O_3 rich layer [39,40]. However, because of the faster diffusion of Ti through Cr_2O_3, it is observed that TiO_2 was also formed at the outermost part of the outer layer. A similar enrichment of TiO_2 above a Cr_2O_3 layer has been observed after the oxidation of Ni-Cr-Al alloys [39,41].

By comparison of Figures 5, 8 and 13, it is evident that preoxidation has a positive effect with respect to reducing the corrosion attack on Nimonic 80A, under laboratory conditions mimicking biomass firing. The fact that no significant attack occurred on the preoxidation layer containing a Cr/Ti-oxide is intriguing because previous work has suggested that KCl can destroy Cr-rich oxides according to reaction (1) [6,27,30]. With appreciable amount of KCl vapour (> 10^{-6} atm) [42] being generated at 560 °C, this reaction is highly favourable with a Gibbs free energy change (ΔG^0) of -60.3 kJmol^{-1}(HCl) at 560 °C [43,44].

$$\frac{1}{4}Cr_2O_3(s) + KCl(s,g) + \frac{3}{8}O_2(g) + \frac{1}{2}H_2O(g) \rightleftharpoons \frac{1}{2}K_2CrO_4(s) + HCl(g) \qquad (1)$$

However, for a similar reaction involving TiO_2 (rutile), thermodynamic calculations with FactSage [43,44] reveal that at 560 °C, reaction 2 is accompanied with a positive Gibbs free energy change (ΔG^0) of 123.7 kJmol^{-1} (solid KCl) and 26.8 kJmol^{-1} (gaseous KCl), making such a reaction to be thermodynamically unfavoured.

$$\frac{1}{2}TiO_2(s) + KCl(s,g) + \frac{1}{2}H_2O(g) \rightleftharpoons \frac{1}{2}K_2TiO_3(s) + HCl(g) \qquad (2)$$

Hence, it appears that the thin TiO_2 enriched layer in the outermost part of the outer oxide layer (Figures 1c and 2c) rendered protection against corrosion attack. Although this is in agreement with a previous study [31] in which no reactivity was observed for a mixture of TiO_2 and KCl exposed at 650 °C for 15 h to an atmosphere containing 5% O_2 + 15% H_2O, corrosion exposures for longer durations than 168 hours will be necessary to evaluate the long term resistance offered by the TiO_2 enriched layer.

The severe corrosion attack observed on non-preoxidized samples (Figures 5 and 13) can be explained by the absence of a protective oxide on the samples, prior to the corrosion exposures. The tendency of reaction (1) to occur during the initial stages of the exposures, due to the absence of a protective Ti-rich surface oxide may have resulted in formation of non-protective oxides that allowed ingress of Cl-containing species. It has to be noted that HCl can be released from reaction (1), and from the reaction between KCl and SO_2 in the gas phase (reaction 3) [34,45,46], forming K_2SO_4 which was identified on samples after the corrosion exposures (Figures 5b, 6a, b, 8 and 11a, b). Upon dissociation of HCl via the Deacon process [47–49], Cl_2 is generated and can propagate the corrosion attack by chlorination of the alloying elements at the corrosion front, where the oxygen partial pressure is relatively low. Although the HCl originally present in the gas mixture also has the tendency of

inducing chlorination attack by itself, previous studies [50,51] have shown that this has a lower influence on the degree of corrosion attack, compared to corrosion attack in the presence of KCl deposits.

$$2KCl(s) + SO_2(g) + H_2O(g) + \frac{1}{2}O_2(g) \rightleftharpoons K_2SO_4(s) + 2HCl(g) \qquad (3)$$

Results from plan view characterization (Figures 6 and 11) also reveal that the preoxidation layer has an effect on the sulphation process (i.e., reaction 3) as there was less accumulation of K_2SO_4 around the KCl deposit particles on preoxidized samples (Figure 11a and b), compared to non-preoxidized samples (Figure 6a and b). At low temperatures (such as in the present study), it has to be noted that a vital intermediate step in reaction (3) involves the oxidation of SO_2 to SO_3, which is often catalyzed by oxides [45,52,53]. This is substantiated by the fact that KCl is converted to sulphate at the deposit/flue gas interface (as would be expected due to high SO_2 content in the flue gas) and at the oxide/deposit interface, but remains unconverted within the bulk of the deposit [32,34]. Based on previous studies, Fe_2O_3, Cr_2O_3, V_2O_5, CaO and CuO exhibit better catalytic activity for the SO_2-SO_3 conversion than oxides of Ti, Si, Th, U, Ce, W, Sn, As and Mo [54–57]. Thus, the TiO_2 in the outer layer of the preoxidized samples may have hindered the oxidation of SO_2 to SO_3 during the corrosion exposure, and thus, the sulphation process (Figure 6) thereby reducing HCl formation which propagates the corrosion attack. Therefore in addition to the unfavourable reaction between TiO_2 and KCl deposits (reaction 2), the presence of TiO_2 in the preoxidation layer may have contributed to the observed resistance to corrosion attack, because of its negative influence on the generation of HCl close to the alloy surface. This dual effect against corrosion under biomass firing conditions suggests promising potentials for surface modification approaches that can promote the formation of TiO_2 surface layers. Corrosion exposures for longer durations will also be required to clarify this.

From Figures 5b and 13b, it is evident that the total chlorine partial pressure (p_{Cl_2}) resulting from dissociation of the HCl in the gas mixture, in addition to that from reactions (1) and (3), was sufficient to cause chlorination of the alloying elements, Ni, Cr, Ti and Al in the non-preoxidized samples. According to thermodynamic calculations with FactSage [43,44], metal chlorides resulting from chlorination of Ti and Al will require a lower p_{O_2} for conversion to their oxides, and this correlates with the presence of Ti and Al rich oxides, closer to the corrosion front as observed in Figures 5b and c, as well as in Figure 13b. In contrast, Ni and Cr-rich oxide precipitates (whose corresponding metal chlorides require relatively higher p_{O_2} conditions for conversion to oxides), were mostly observed in the outermost regions of the corrosion product and in some cases, in a mixture with the K, S, O rich layer above the porous oxide (Figures 5a and 13a). It is important to note that even though the low p_{O_2} condition required for conversion of Ti and Al chlorides appears to have caused formation of their oxides above the alloy bulk (Figures 5b and c), the porous and heterogeneous morphology of the entire corrosion product suggests that such oxides will not give adequate protection against further corrosion attack in a manner similar to the previously reported halogen effect [58].

5. Conclusions

The influence of preoxidation of Nimonic 80A on its high temperature corrosion performance under laboratory conditions mimicking biomass firing at 560 ºC was investigated. From the observed results, the following conclusions are made.

1. Without preoxidation, Nimonic 80A suffers corrosion resulting in the formation of an inner oxide of Ti and Al and an outer porous oxide containing Ni, Cr, and Al. The outer porous oxide is submerged in a layer of K_2SO_4 ensuing from the reaction of the KCl deposit with SO_2 in the gas mixture.
2. Preoxidation of Nimonic 80A at 900 ºC for 168 h results in an outward growing TiO_2 and Cr_2O_3 containing oxide in which Ti is enriched in the outermost part, and an internal oxidation zone in which Al and Ti are oxidized. The preoxidation atmosphere (with or without water vapour) seem not to affect the composition, morphology and thickness of the pre-oxidized surface layers.
3. The reaction between KCl and TiO_2 is thermodynamically unfavourable, and in addition, TiO_2 is a poor catalyst for HCl formation from the sulphation reaction. Therefore, TiO_2 in the outer part of the preoxidation layer protects against corrosion attack on the alloy.

6. Acknowledgements

This work is part of the Danish Strategic Research Centre, Power Generation from Renewable Energy (GREEN). The authors acknowledge funding from the Danish council for Strategic Research.

References

[1] M. Montgomery, S.A. Jensen, U. Borg, O. Biede, T. Vilhelmsen, Experiences with high temperature corrosion at straw-firing power plants in Denmark, Mater. Corros. 62 (2011) 593–605.

[2] W.B.A. Sharp, Superheater Corrosion in Biomass Boilers : Today's Science and Technology, 2011.

[3] F.J. Frandsen, Utilizing biomass and waste for power production—a decade of contributing to the understanding, interpretation and analysis of deposits and corrosion products, Fuel. 84 (2005) 1277–1294.

[4] S. V. Vassilev, D. Baxter, L.K. Andersen, C.G. Vassileva, An overview of the chemical composition of biomass, Fuel. 89 (2010) 913–933.

[5] F.J. Frandsen, Ash Formation, Deposition and Corrosion when Utilizing Straw for Heat and Power Production, Dr. Techn. Thesis, Department of Chemical and Biochemical Engineering, Technical Univeristy of Denmark. ISBN: 9788792481405, Kongens Lyngby, 2011.

[6] R.A. Antunes, M.C.L. de Oliveira, Corrosion in biomass combustion: A materials selection analysis and its interaction with corrosion mechanisms and mitigation strategies, Corros. Sci. 76 (2013) 6–26.

[7] S. Kiamehr, K.V. Dahl, M. Montgomery, M.A.J. Somers, KCl-induced high temperature corrosion of selected commercial alloys. Part II: alumina and silica-formers, Mater. Corros. 67 (2016) 26–38.

[8] S. Kiamehr, K.V. Dahl, M. Montgomery, M.A.J. Somers, KCl-induced high temperature corrosion of selected commercial alloys. Part I: chromia-formers, Mater. Corros. 66 (2015) 1414–1429.

[9] J. Lehmusto, P. Yrjas, B.-J. Skrifvars, M. Hupa, High temperature corrosion of superheater steels by KCl and K2CO3 under dry and wet conditions, Fuel Process. Technol. 104 (2012) 253–264.

[10] C. Pettersson, J. Pettersson, H. Asteman, J.-E. Svensson, L.-G. Johansson, KCl-induced high temperature corrosion of the austenitic Fe–Cr–Ni alloys 304L and Sanicro 28 at 600°C, Corros. Sci. 48 (2006) 1368–1378.

[11] F. Wang, Y. Shu, Influence of Cr Content on the Corrosion of Fe – Cr Alloys : The Synergistic Effect of NaCl and Water Vapor, Oxid. Met. 59 (2003) 201–214.

[12] N. Israelsson, K. Hellström, J.-E. Svensson, L.-G. Johansson, KCl-Induced Corrosion of the FeCrAl Alloy Kanthal ® AF at 600 °C and the Effect of H2O, Oxid. Met. 83 (2015) 1–27.

[13] M. Spiegel, A. Zahs, H.J. Grabke, Fundamental aspects of chlorine induced corrosion in power plants, Mater. High Temp. 20 (2003) 153–159.

[14] T. Hussain, T. Dudziak, N.J. Simms, J.R. Nicholls, Fireside Corrosion Behavior of HVOF and Plasma-Sprayed Coatings in Advanced Coal/Biomass Co-Fired Power Plants, J. Therm. Spray Technol. 22 (2013) 797–807.

[15] M.. Uusitalo, P.M.. Vuoristo, T.. Mäntylä, High temperature corrosion of coatings and boiler steels in reducing chlorine-containing atmosphere, Surf. Coatings Technol. 161 (2002) 275–285.

[16] J. Metsäjoki, E. Huttunen-Saarivirta, T. Lepistö, Corrosion of Aluminized and Uncoated 9–12% Cr Boiler Steels in Simulated Biomass andWaste Combustion Conditions, High Temp. Mater. Process. 30 (2011) 181–191.

[17] S. Paul, M.D.F. Harvey, Corrosion Testing of Ni Alloy HVOF Coatings in High Temperature Environments for Biomass Applications, J. Therm. Spray Technol. 22 (2012) 316–327.

[18] M.. Uusitalo, P.M.. Vuoristo, T.. Mäntylä, High temperature corrosion of coatings and boiler steels below chlorine-containing salt deposits, Corros. Sci. 46 (2004) 1311–1331.

[19] X. Li, Z. Liu, H. Li, Y. Wang, B. Li, Investigations on the behavior of laser cladding Ni–Cr–Mo alloy coating on TP347H stainless steel tube in HCl rich environment, Surf. Coatings Technol. 232 (2013) 627–639.

[20] P.S. Sidky, M.G. Hocking, The effect of pre-oxidation and thermal cycling on the corrosion behaviour of Fe-Cr-Al-based alloys in a coal gasifier atmosphere, Corros. Sci. 29 (1989) 735–765.

[21] M.F. Pillis, L.V. Ramanathan, Effect of pre-oxidation on high temperature sulfidation

behavior of FeCr and FeCrAl alloys, Mater. Res. 7 (2004) 97–102.

[22] M.F. Stroosnijder, V. Guttmann, H. Buscail, J.H.W. de Wit, The effect of pre-oxidation and the influence of deformation on the corrosion behaviour of two heat resistant steels in a sulphur-oxygen-carbon bearing environment, Corros. Sci. 36 (1994) 207–219.

[23] M.M. Stack, F.H. Stott, G.C. Wood, The effect of pre-oxidation of chromia and alumina forming alloys on erosion in laboratory simulated fluidized-bed conditions, Corros. Sci. 33 (1992) 965–983.

[24] S. Sheybany, D.L. Douglass, The effect of preoxidation of some Ni, Fe, and Co-Base alloys on subsequent sulfidation at 982 oC in sulfur vapor, Oxid. Met. 30 (1988) 433–463.

[25] J. Lehmusto, P. Yrjas, M. Hupa, The Effect of Pretreatment on the Corrosion Resistance of Superheater Materials, Solid State Phenom. 227 (2015) 309–312.

[26] N. Israelsson, J. Engkvist, K. Hellström, M. Halvarsson, J.-E. Svensson, L.-G. Johansson, KCl-Induced Corrosion of an FeCrAl Alloy at 600 °C in O2 + H2O Environment: The Effect of Pre-oxidation, Oxid. Met. 83 (2015) 29–53.

[27] T.J. Pan, H.T. Ma, Y.S. Li, Surface layer evolutions of pre-oxidised Fe–30Cr alloy induced by gaseous KCl, Corros. Eng. Sci. Technol. 46 (2011) 499–504.

[28] P. Viklund, R. Pettersson, HCl-Induced High Temperature Corrosion of Stainless Steels in Thermal Cycling Conditions and the Effect of Preoxidation, Oxid. Met. 76 (2010) 111–126.

[29] H. Asteman, M. Spiegel, Investigation of the HCl (g) attack on pre-oxidized pure Fe, Cr, Ni and commercial 304 steel at 400°C, Corros. Sci. 49 (2007) 3626–3637.

[30] J. Pettersson, H. Asteman, J.-E. Svensson, L.-G. Johansson, KCl Induced Corrosion of a 304-type Austenitic Stainless Steel at 600°C; The Role of Potassium, Oxid. Met. 64 (2005) 23–41.

[31] S. Kiamehr, K. V Dahl, T.N. Lomholt, T.L. Christiansen, M.A.J. Somers, High Temperature Corrosion due to Biomass Firing : A Study on the Reactivity between Potassium Chloride and Oxides, in: Int. Symp. High-Temperature Oxid. Corros., The Iron and Steel Institute of Japan, Hokkaido, 2014: pp. 144–147.

[32] S.C. Okoro, M. Montgomery, F.J. Frandsen, K. Pantleon, Effect of Water Vapor on High-Temperature Corrosion under Conditions Mimicking Biomass Firing, Energy & Fuels. 29 (2015) 5802–5815.

[33] S.C. Okoro, F. Niessen, M. Villa, D. Apel, M. Montgomery, F.J. Frandsen, K. Pantleon, Complementary Methods for the Characterization of Corrosion Products on a Plant-Exposed Superheater Tube, Metallogr. Microstruct. Anal. 6 (2017) 22–35.

[34] S.C. Okoro, M. Montgomery, F.J. Frandsen, K. Pantleon, High Temperature Corrosion under Laboratory Conditions Simulating Biomass-Firing: A Comprehensive Characterization of Corrosion Products, Energy & Fuels. 28 (2014) 6447–6458.

[35] A. Chyrkin, R. Pillai, H. Ackermann, H. Hattendorf, S. Richter, W. Nowak, D. Grüner, W.J. Quadakkers, Modeling carbide dissolution in alloy 602 CA during high temperature

oxidation, Corros. Sci. 96 (2015) 32–41.

[36] C.S. Giggins, F.S. Pettit, Oxidation of Ni-Cr-Al Alloys Between 1000° and 1200°C, J. Electrochem. Soc. 118 (1971) 1782.

[37] E.J. Opila, N.S. Jacobson, D.L. Myers, E.H. Copland, Predicting oxide stability in high-temperature water vapor, JOM. 58 (2006) 22–28.

[38] H. Asteman, J.-E. Svensson, L.-G. Johansson, Oxidation of 310 steel in H2O/O2 mixtures at 600 °C: the effect of water-vapour-enhanced chromium evaporation, Corros. Sci. 44 (2002) 2635–2649.

[39] D.W. Yun, S.M. Seo, H.W. Jeong, Y.S. Yoo, The cyclic oxidation behaviour of Ni-based superalloy GTD-111 with sulphur impurities at 1100°C, Corros. Sci. 90 (2015) 392–401.

[40] H.J.T. Ellingham, Transactions and Communications: Reducibilty of oxides and sulphides in metallurgical processes, J. Soc. Chem. Ind. 63 (1944) 125–133.

[41] K.A. Al-hatab, M.A. Al-bukhaiti, U. Krupp, M. Kantehm, Cyclic Oxidation Behavior of IN 718 Superalloy in Air at High Temperatures, Oxid. Met. 75 (2011) 209–228.

[42] J. Pettersson, N. Folkeson, L.-G. Johansson, J.-E. Svensson, The Effects of KCl, K2SO4 and K2CO3 on the High Temperature Corrosion of a 304-Type Austenitic Stainless Steel, Oxid. Met. 76 (2011) 93–109.

[43] What's New in FactSage 7.0, (2015). http://www.crct.polymtl.ca/fact/facthelp/FS70New.htm (accessed June 2, 2016).

[44] C.W. Bale, E. Bélisle, P. Chartrand, S.A. Decterov, G. Eriksson, K. Hack, I.-H. Jung, Y.-B. Kang, J. Melançon, A.D. Pelton, C. Robelin, S. Petersen, FactSage thermochemical software and databases — recent developments, Calphad. 33 (2009) 295–311.

[45] Z. Hu, X. Wang, Z. Wang, Y. Wang, H. Tan, Segmented Kinetic Investigation on Condensed KCl Sulfation in SO 2 /O 2 /H 2 O at 523–1023 K, Energy & Fuels. 28 (2014) 7560–7568.

[46] L.W. Sengeløv, T.B. Hansen, C. Bartolome, H. Wu, K.H. Pedersen, F.J. Frandsen, A.D. Jensen, P. Glarborg, Sulfation of Condensed Potassium Chloride by SO 2, Energy & Fuels. 27 (2013) 3283–3289.

[47] H.J. Grabke, E. Reese, M. Spiegel, The effects of chlorides, hydrogen chloride, and sulfur dioxide in the oxidation of steels below deposits, Corros. Sci. 37 (1995) 1023–1043.

[48] A. Zahs, M. Spiegel, H. Grabke, The influence of alloying elements on the chlorine-induced high temperature corrosion of Fe-Cr alloys in oxidizing atmospheres, Mater. Corros. 50 (1999) 561–578.

[49] H. Over, R. Schomäcker, What Makes a Good Catalyst for the Deacon Process?, ACS Catal. 3 (2013) 1034–1046.

[50] S.C. Okoro, S. Kiamehr, M. Montgomery, F.J. Frandsen, K. Pantleon, Effect of flue gas composition on deposit induced high temperature corrosion under laboratory conditions mimicking biomass firing. Part I: Exposures in oxidizing and chlorinating atmospheres,

Mater. Corros. 68 (2017) 499–514.

[51] S.C. Okoro, S. Kiamehr, M. Montgomery, F.J. Frandsen, K. Pantleon, Effect of flue gas composition on deposit induced high temperature corrosion under laboratory conditions mimicking biomass firing. Part II: Exposures in SO 2 containing atmospheres, Mater. Corros. 68 (2017) 515–528.

[52] K. Iisa, Y. Lu, K. Salmenoja, Sulfation of Potassium Chloride at Combustion Conditions, Energy & Fuels. 13 (1999) 1184–1190.

[53] J.E. García-Herrera, J.M. Alvarado-Orozco, J. Muñoz-Saldaña, L. Garcia-Fresnillo, G.H. Meier, The Effect of Different SO2/SO3 Catalytic Media on High-Temperature Corrosion Processes (Hot Corrosion, Fireside Corrosion, Sulfidation–Oxidation), Oxid. Met. (2015) 233–240.

[54] O. V. Krylov, Catalysis by Nonmetals: Rules for Catalyst Selection, Academy press, New York, 1970.

[55] L.P. Belo, L.K. Elliott, R.J. Stanger, R. Spörl, K. V. Shah, J. Maier, T.F. Wall, High-Temperature Conversion of SO2 to SO3: Homogeneous Experiments and Catalytic Effect of Fly Ash from Air and Oxy-fuel Firing, Energy & Fuels. 28 (2014) 7243–7251.

[56] T.L. Jørgensen, H. Livbjerg, P. Glarborg, Homogeneous and heterogeneously catalyzed oxidation of SO2, Chem. Eng. Sci. 62 (2007) 4496–4499.

[57] P. Marier, H.P. Dibbs, The catalytic conversion of SO2 to SO3 by fly ash and the capture of SO2 and SO3 by CaO and MgO, Thermochim. Acta. 8 (1974) 155–165.

[58] M. Schütze, G. Schumacher, F. Dettenwanger, U. Hornauer, E. Richter, E. Wieser, W. Möller, The halogen effect in the oxidation of intermetallic titanium aluminides, Corros. Sci. 44 (2002) 303–318.